

A Predictive First-Principles Framework of Chiral Charge Density Waves

Sen Shao ^{*,1}, Wei-Chi Chiu ^{*,2,3}, Md Shafayat Hossain ^{*,4}, Tao Hou ¹, Naizhou Wang ¹,
Ilya Belopolski ⁵, Yilin Zhao ¹, Jinyang Ni ¹, Qi Zhang ⁴, Yongkai Li ^{6,7,8}, Jinjin Liu ^{6,7,8},
Mohammad Yahyavi ¹, Yuanjun Jin ¹, Qiange Feng ^{1,9}, Peiyuan Cui ¹, Cheng-Long
Zhang ¹⁰, Yugui Yao ^{6,7}, Zhiwei Wang ^{6,7,8}, Jia-Xin Yin ⁹, Su-Yang Xu ¹¹, Qiong
Ma ^{12,13}, Wei-bo Gao ¹, Arun Bansil ^{†,2,3}, M. Zahid Hasan ^{†,4} and Guoqing Chang ^{†1}

¹*Division of Physics and Applied Physics,*

School of Physical and Mathematical Sciences,

Nanyang Technological University, 21 Nanyang Link, 637371, Singapore

²*Department of Physics, Northeastern University, Boston, MA 02115, USA*

³*Quantum Materials and Sensing Institute,*

Northeastern University, Burlington, MA 01803, USA

⁴*Laboratory for Topological Quantum Matter and Advanced Spectroscopy (B7),*

Department of Physics, Princeton University, Princeton, New Jersey 08544, USA

⁵*RIKEN Center for Emergent Matter Science (CEMS), Wako, Saitama 351-0198, Japan*

⁶*Centre for Quantum Physics, Key Laboratory of Advanced Optoelectronic,*

Quantum Architecture and Measurement (MOE), School of Physics,

Beijing Institute of Technology, Beijing 100081, China

⁷*Beijing Key Lab of Nanophotonics and Ultrafine Optoelectronic Systems,*

Beijing Institute of Technology, Beijing 100081, China

⁸*Material Science Center, Yangtze Delta Region Academy*

of Beijing Institute of Technology, Jiaxing 314011, China

⁹*Department of Physics, Southern University of Science and Technology,*

Shenzhen, Guangdong 518055, China

¹⁰*Beijing National Laboratory for Condensed Matter Physics,*

Institute of Physics, Chinese Academy of Sciences, Beijing 100190, China

¹¹*Department of Chemistry and Chemical Biology,*

Harvard University, Cambridge, MA, USA

¹²*Department of Physics, Boston College, Chestnut Hill, MA, USA*

¹³*CIFAR Azrieli Global Scholars program, CIFAR, Toronto, Canada*

(Dated: November 7, 2024)

*These authors contributed equally to this work.

†Corresponding emails: guoqing.chang@ntu.edu.sg, mzh Hasan@princeton.edu, ar.bansil@northeastern.edu

ABSTRACT

Implementing and tuning chirality is fundamental in physics, chemistry, and material science. Chiral charge density waves (CDWs), where chirality arises from correlated charge orders, are attracting intense interest due to their exotic transport and optical properties. However, a general framework for predicting chiral CDW materials is lacking, primarily because the underlying mechanisms remain elusive. Here, we address this challenge by developing the first comprehensive predictive framework, systematically identifying chiral CDW materials via first-principles calculations. The key lies in the previously overlooked phase difference of the CDW Q-vectors between layers, which is linked to opposite collective atomic displacements across different layers. This phase difference induces a spiral arrangement of the Q-vectors, ultimately giving rise to a chiral structure in real space. We validate our framework by applying it to the kagome lattice AV_3Sb_5 ($A = K, Rb, Cs$), successfully predicting emergent structural chirality. To demonstrate the generality of our approach, we extend it to predict chiral CDWs in the triangular-lattice $NbSe_2$. Beyond material predictions, our theory uncovers a universal and unprecedented Hall effect in chiral CDW materials, occurring without external magnetic fields or intrinsic magnetization. Our experiments on CsV_3Sb_5 confirm this prediction, observing a unique signature where the Hall conductivity's sign reverses when the input current is reversed, a phenomenon distinct from known Hall effects. Our findings elucidate the mechanisms behind chiral CDWs and open new avenues for discovering materials with unconventional quantum properties, with potential applications in next-generation electronic and spintronic devices.

Chirality, a fundamental geometrical property, has profound implications across the physical, chemical as well as the biological sciences [1–11]. Chirality plays a pivotal role in elucidating the nature of fundamental forces in particle physics and in understanding a wide range of exotic phenomena in condensed matter systems [4–21]. Traditionally, chirality in materials is fixed during chemical synthesis, posing significant challenges for controlling chirality in practical applications. However, recent advancements have revealed that chirality can also emerge from low-energy physical processes, enabling energy-efficient control of material chirality. A notable example is chiral charge density waves (CDWs), where chirality arises from correlated charge orders [22–32]. Fast electrical and optical control and manipulation of chirality have been realized in chiral CDW phases of 1T-TiSe₂/1T-TaS₂ [24–29]. Recent studies of AV_3Sb_5 ($A = K, Rb, Cs$) have further demonstrated that chiral CDWs can support many unconventional

properties in transport, optics, and superconductivity [30–33].

Despite significant research interest in correlation-driven emergent chirality, the number of materials supporting the chiral CDW phase remains limited. The discovery of chiral CDWs in 1T-TiSe₂ and AV₃Sb₅ (A = K, Rb, Cs) family has resulted from experimental serendipity rather than rational materials design considerations [22, 30, 31]. A possible strategy is to realize the chiral CDW by inducing electronic chirality without requiring a chiral atomic lattice [23, 26]. While CDWs can break crystal symmetries [34], achieving overall structural chirality in this way is particularly challenging as it requires breaking mirror and inversion symmetries. A robust mechanism by which correlated charge orders can induce chirality in the atomic lattice is more desirable but remains elusive. In the existing chiral CDW materials, while first principles studies have proposed CDW supercell size consistent with the corresponding experimental observations, structural chirality has not been realized in the proposed structures [35–37]. This gap not only impedes the discovery of new chiral CDW materials but also limits the ability to predict the unique quantum effects induced by chiral CDWs.

Mechanism of inducing structural chirality via CDW

To explore the mechanism of inducing structural chirality via a charge density wave (CDW), we start by revisiting the one-dimensional (1D) atomic chain with Peierls distortion. As illustrated in Fig. 1a, centered in the coordinate system, chains 1 and 2 exhibit opposite collective atomic displacements. Due to translational symmetry, both chains are equivalent and share the same CDW Q-vector. However, when chains 1 and 2 are stacked to create a two-dimensional (2D) material with weak, nonzero inter-chain coupling, the relative atomic displacement between the chains becomes important, influencing the CDW supercells and associated symmetries. For instance, stacking identical chains in the y -direction preserves symmorphic mirror symmetry between chains, whereas stacking chain 1 with chain 2 introduces a glide mirror symmetry (Fig. S1). Recognizing the role of relative atomic displacements in symmetry breaking, we introduce different phases of Q-vectors, Q_x and $Q_{\bar{x}}$, to represent the opposite displacements of the two chains (Fig. 1a right-panel).

Building on this concept, we extend it to higher-dimensional cases by stacking 2D CDW layers into a quasi-2D, three-dimensional (3D) system. We assume that the coupling between different layers is so weak that it does not affect the Q-vectors within each layer. For instance, in a hexagonal Brillouin zone (BZ), there will be three Q-vectors linked by three- or six-fold rotational symmetry: Q_1 , Q_2 , and Q_3 (Fig. 1b). Taking relative atomic displacement in real space into account, we introduce $Q_{\bar{1}}$, $Q_{\bar{2}}$, and $Q_{\bar{3}}$, which represent opposite phases in

each respective direction. Combinations of these wavevectors, along with phase information, correspond to eight possible collective atomic displacements in real space. For instance, defining one possible displacement as a reference $Q_1Q_2Q_3$, the combination $Q_{\bar{1}}Q_2Q_3$ indicates a layer where the relative atomic displacement in direction one is opposite to the reference, while it remains the same in directions two and three. When we stack layers with Q-vectors of the same phase, there will be a uniform charge density across layers, preserving existing symmetry elements and yielding an achiral structure. However, when we stack three layers with Q-vectors with different phases, structural chirality may appear. For instance, by placing $Q_1Q_2Q_3$ in layer 1, $Q_{\bar{1}}Q_2Q_3$ in layer 2, and $Q_1Q_{\bar{2}}Q_3$ in layer 3 forms a spiral pattern of Q-vectors, indicating the structural chirality in real space (Fig. 1b).

Predicting structural chirality in kagome lattices AV_3Sb_5 ($A = K, Rb, Cs$)

Next, we apply this mechanism in real material CsV_3Sb_5 through first-principle calculations to validate its availability and predictability. The pristine phase of CsV_3Sb_5 is in a high-symmetric space group $P6/mmm$, possessing 6, 3, 2, \mathcal{M}_{100} , \mathcal{M}_{010} , \mathcal{M}_{001} , \mathcal{M}_{210} , \mathcal{M}_{120} , \mathcal{M}_{110} , $\mathcal{M}_{\bar{1}\bar{1}0}$ and $\bar{1}$ symmetries (Fig. 2a). Within each layer, there are two possible distorted 2×2 CDW structures: the star of David (SoD) and the inverse star of David (ISD), induced by Q-vectors $Q_i/Q_{\bar{i}}$ ($i = 1, 2, 3$) [35]. Accounting for all possible phase differences across the three directions, we identified eight configurations per layer: four corresponding to ISD and four to SoD (Figs. S2-S3).

We use the ISD configuration in Fig. 2b as a reference, defined by Q-vector arrangement $Q_1Q_2Q_3$. Accordingly, the configuration in Fig. 2c is represented as $Q_{\bar{1}}Q_2Q_3$, indicating that the displacements along directions one and two are opposite to the reference, while the displacement along direction three remains the same.

We begin by examining 3D structures that contain two kagome layers per unit cell. Considering all possible relative displacements, represented by the phases of Q-vectors within the $2 \times 2 \times 2$ CDW supercell, we identified thirty-six distinct structures (Table S1). Inputting all these structures into first-principle calculations, we find that the stacking of $Q_1Q_2Q_3$ and $Q_{\bar{1}}Q_2Q_3$ ISD layers exhibit the lowest energy. Notably, all structures with ISD patterns have lower energy than that with SoD patterns (Table S1), consistent with previous studies [35]. Therefore, in the subsequent study of $2 \times 2 \times 3$ and $2 \times 2 \times 4$ superlattices, we focus exclusively on combining ISD patterns.

We then study unit cells with more than two layers. Based on all possible displacements of the ISD patterns, we identified fifteen $2 \times 2 \times 3$ structures and forty-one $2 \times 2 \times 4$ structures.

Our exhaustive first-principle calculations yielded two chiral structures in $2\times 2\times 3$ cell and one chiral structure in $2\times 2\times 4$ cell (Tables S2-S4). Figure 2d demonstrates one of $2\times 2\times 3$ CDW-driven chiral structures in space group $P6_22$, where layer 1 is denoted as $Q_1Q_2Q_3$, layer 2 as $Q_1^-Q_2^-Q_3^-$, and layer 3 as $Q_1Q_2Q_3$. The thermodynamic stability analysis confirms that these chiral structures possess lower energy than the pristine phase. The calculation of phonon spectra also demonstrates their dynamic stability (Fig. 2e). Applying the same methodology, we also find CDW-driven chiral structures of KV_3Sb_5 and RbV_3Sb_5 (Table S5-S10).

Next, we compare our predicted CDW structures with previous experimental observations in AV_3Sb_5 ($A=K, Rb$ and Cs) family. The simulated surface charge distributions of our proposed chiral CDWs manifest spiral patterns (Fig. 2f), which are also reflected in previous STM images [30]. Additionally, the energies of CDW-driven $2\times 2\times 2$ achiral and $2\times 2\times 4$ chiral structures are nearly degenerate in the calculation (Tables S1, S3), suggesting competition between the two phases during crystal growth. This competition has been observed experimentally, with some experiments exclusively producing the $2\times 2\times 2$ phase [38], others the $2\times 2\times 4$ phase [39], and some documenting a coexistence of both phases [40]. This is also reflected in conflicting experimental reports regarding mirror symmetries. Some studies indicate the absence of in-plane mirror symmetries [30–32], while others report their presence in the CDW phase [41]. Our calculations suggest that this experimental discrepancy may stem from (near) degenerate CDW phases. Variations in inevitable perturbations, such as strain across different experimental samples, could lead to the preferential stabilization of one CDW phase over the others. This could provide a plausible explanation for the seemingly contradictory experimental results [30–32, 41–44].

We want to further highlight that the $2\times 2\times 3$ structures predicted in this work are also degenerate with the other $2\times 2\times 2$ achiral and $2\times 2\times 4$ structures, indicating they are also possible ground states. The main difference between $2\times 2\times 3$ and $2\times 2\times 4$ supercells is that the $2\times 2\times 4$ breaks three- and six-fold rotation symmetry, while $2\times 2\times 3$ still preserve a six-fold screw rotation symmetry. Yet, on the surface of $2\times 2\times 3$ supercell, the six-fold screw rotation is also broken with only two-fold rotation symmetry preserved. We expect further experiments may observe the $2\times 2\times 3$ phase predicted here.

Scheme of prediction chiral CDW materials via first-principles calculations

Having demonstrated our method’s capability to predict CDW-induced structural chirality in AV_3Sb_5 ($A = K, Rb, Cs$), we now extend it to predict potential chiral CDWs not yet observed experimentally. Here, we use transition metal dichalcogenides (TMDs) as an example, where

chiral charge density waves (CDWs) have been observed in 1T-TiSe₂ and 1T-TaS₂ [24–29]. Due to the structural and electronic similarities across the TMDs, there is potential for other TMDs to support emergent chirality. We choose the triangular lattice 1T-NbSe₂ ($P\bar{3}m1$) as our example, whose 2D chiral CDW has been reported experimentally [45] but 3D chiral CDW not yet (Fig. 3a).

To predict the chiral CDW in 1T-NbSe₂, we employ a three-step approach. First, we perform first-principles calculations to determine the phonon spectra of single layer 1T-NbSe₂, identifying structural instability through the presence of negative frequencies. From phonon calculation, we obtain conventional triple Q-vectors for the single layer 1T-NbSe₂, which indicates the presence of a stable $\sqrt{13}\times\sqrt{13}$ supercell. In the second step, we apply our mechanism as illustrated in Figs. 1-2, introducing varying phases across layers to explore potential chiral CDW phases in bulk 1T-NbSe₂. Specifically, we first define the Q-vector phases to represent opposite atomic displacements in each direction: $Q_1/Q_{\bar{1}}$, $Q_2/Q_{\bar{2}}$, and $Q_3/Q_{\bar{3}}$ (Fig. S4). The combinations of different phases in three directions generates eight possible patterns for each layer (Fig. S5). Stacking these patterns in a spiral Q-vector arrangement breaks all mirror and inversion symmetries, forming a chiral CDW phase. For 1T-NbSe₂, this can be exemplified by the $\sqrt{13}\times\sqrt{13}\times 3$ chiral structure, illustrated in Fig. 3c, which is generated by incorporating patterns $Q_1Q_2Q_3$, $Q_{\bar{1}}Q_2Q_3$, and $Q_{\bar{1}}Q_{\bar{2}}Q_3$ into a single unit cell. In the third step, we verify the potential chiral CDW through first-principles calculations. Our thermodynamic and dynamic stability analyses confirm that this chiral structure is more stable and energetically favorable (Figs. 3d-3e). Thus, our calculations predict potential CDW-driven chiral phases in 3D 1T-NbSe₂ at low temperatures (more chiral CDWs see Table S11).

This three-step framework offers a comprehensive approach for predicting CDW-driven chiral structures in layered or quasi-layered quantum materials, as outlined in Fig. 3f. While Steps I and III are well-established in previous studies [35, 46], a critical gap remains as the underlying mechanisms of chiral CDWs are elusive, limiting the predictive power of first-principles calculations for chiral CDW materials. By identifying the previously overlooked phase differences in CDW Q-vectors across layers and their spiral configurations, our work bridges this gap through the introduction of Step II, thus significantly accelerating the discovery of chiral CDW materials.

Correlation-driven spin-anomalous dual-Hall effect in Chiral CDW materials

The correlation-driven structural chirality mechanism presented in this work not only facilitates the discovery of additional chiral CDW materials but also enables the prediction of their

unique quantum effects. Beyond inducing structural chirality, we predict that our chiral CDW mechanism can give rise to a new correlation-driven “anomalous” Hall effect in non-magnetic, metallic chiral CDW systems without external magnetic field.

Notably, CDW materials can open a continuous band gap at low temperatures while leaving electron and hole pockets at the Fermi level. In other words, chiral CDW materials can remain metallic and “activate” spin-Hall effects due to the correlation-driven P -symmetry breaking. Consequently, when an unpolarized electric current is injected into a slab of chiral CDW material, a transverse spin current is generated, leading to opposite spin accumulation at the material’s two boundaries (Fig. 4a, left). These spin accumulations induce local magnetism and break time-reversal symmetry (T -symmetry) on each surface. Because of the opposing spin accumulation, the Berry curvature on the top and bottom surfaces takes on opposite signs. In systems where PT -symmetry is preserved, the Berry curvature from the two surfaces cancels out (Fig. S6). However, in our case, PT -symmetry is broken due to the correlation-driven P -symmetry breaking prior to spin accumulation. This results in an imbalance in the Berry curvature distribution between the top and bottom surfaces (Fig. 4a middle), leading to a measurable transverse conductivity in chiral CDW materials (Fig. 4a right). Unlike traditional AHE, this effect does not require an external magnetic field or net intrinsic magnetization. As this process involves correlated charge orders, the spin Hall effect, and the anomalous Hall effect (AHE), we introduce the term “spin-anomalous dual-Hall effect”, driven by correlated charge order, to distinguish it from the traditional AHE.

One of the key features of the dual-Hall effect is its unique current-direction-dependent response in Hall conductivity σ_{xy} (or resistivity ρ_{xy}), where the sign of the Hall conductivity reverses with the direction of the current. When the input electric current is reversed from I_x to $-I_x$, the spin accumulation on the boundaries will also be flipped (Fig. 4a bottom). As a result, Berry curvature distribution will change signs in the whole system, and so will the σ_{xy} after the sign changes of input current (Fig. 4a bottom). This behavior stands in stark contrast to other Hall effects, where σ_{xy} is an intrinsic material property and remains unaffected by the direction of the input current.

To numerically illustrate this Hall effect, we constructed a model with the chiral CDW on a square lattice based on our mechanism (more details in the Methods section). In our model, the continuous CDW gap leaves behind electron and hole pockets at the Fermi level after turning on CDW interactions (Fig. 4b top). CDW correlations break P -symmetry, lifting the degeneracy of spin-up and spin-down states as well as the degeneracy of opposite Berry curvature (Fig. 4b bottom). To simulate the local magnetization induced by the spin Hall effect on the surface, we applied opposite Zeeman fields at the boundaries, with field strength proportional to the spin

Hall effect calculated from our model. Our results demonstrate a significant anomalous Hall conductivity in systems with chiral CDWs. (Fig. 4c, top). Moreover, the model also captures the sign reversal in spin accumulation at the boundary and the corresponding sign change in anomalous Hall conductivity σ_{xy} (Fig. 4c, bottom).

We observe a substantial Berry curvature distribution “pinned” near the Fermi level in the correlation-driven spin-anomalous dual-Hall effect (Fig. 4b bottom). Through band folding and hybridization, the CDW induces an unconventional wavefunction geometry near the Fermi level, even if the original bands are topologically trivial, leading to a significant Berry curvature distribution at the Fermi level (Fig. 4b). As a result, we anticipate this Hall effect to be an universal feature of our chiral CDW mechanism in materials with metallic ground states, giving rise to considerable Hall conductivity. Since AV_3Sb_5 ($A = K, Rb, Cs$) is reported to remain metallic at chiral CDW phases, it provides an ideal platform to verify our predictions.

Motivated by this, we conducted Hall effect measurements on CsV_3Sb_5 . A Hall bar device was fabricated using a mechanically exfoliated CsV_3Sb_5 flake with a thickness of approximately 90 nm (inset of Fig. 5a). First, we measured the longitudinal resistivity, ρ_{xx} , which exhibits a clear signature of the CDW transition around $T \simeq 89$ K, consistent with previous reports [31, 47]. Next, we proceeded with the Hall effect measurements. Using the transverse contacts, we measured the transverse resistivity, ρ'_{xy} , as a function of the magnetic field (μ_0H) for two opposite directions of current flow at $T \simeq 5$ K. (Fig. 5b). It is important to note that this data is not antisymmetrized with respect to the magnetic field. Typically, transverse resistivity contains contributions from both Hall resistivity and longitudinal resistivity. Since longitudinal resistivity is not expected to change when the direction of current flow is reversed, but Hall resistivity should, we can extract the Hall resistivity by subtracting $\rho'_{xy}(\mu_0H)$ for the two current directions and dividing the result by 2. The resulting Hall resistivity, ρ_{xy} , as a function of μ_0H is shown in Fig. 5c, where it is evident that ρ_{xy} remains finite and non-zero even at zero field.

To further confirm chiral CDW induces this Hall effect, we investigate the temperature dependence of this effect. We measured ρ'_{xy} as a function of temperature for both current directions and calculated $\rho_{xy}(T)$. The temperature-dependent data is displayed in Fig. 5d. Strikingly, $\rho_{xy}(T)$ exhibits a transition coincident with the CDW transition. Before the CDW transition, ρ_{xy} is nearly zero; however, as the sample approaches T_{CDW} , the Hall resistivity increases, eventually reaching a saturated value slightly below T_{CDW} . This observation clearly indicates that the onset of the finite zero-field Hall effect is closely tied to the CDW transition, establishing a direct link between the chiral CDW order and the observed dual-Hall effect.

In summary, our study reveals a mechanism for achieving structural chirality through charge

density waves (CDWs). This approach is readily adaptable to first-principles calculations, facilitating the robust prediction of new families of chiral CDW materials. Our work has the potential to accelerate not only the experimental discovery of these materials but also the exploration of unique quantum effects driven by chiral CDWs. A notable example is our prediction and experimental validation of a zero-field, zero-magnetization Hall effect, which offers a distinct advantage over both conventional and anomalous Hall effects for applications in quantum devices that are sensitive to magnetization or magnetic fields. This new Hall effect also displays unique chirality-locking behavior, where the sign of the Hall conductivity (or resistivity) depends on the structural chirality (Fig. S7), providing a tunable mechanism through chirality control. Our work highlights the role of structural chirality in chiral CDWs and introduces a spiral Q-vector mechanism stemming from hidden phase differences across layers. This mechanism, in principle, can also be extended naturally to charge chirality. The interplay between correlation-driven structural chirality and charge chirality may lead to new phenomena, warranting further theoretical and experimental investigation.

-
- [1] Watson, J. D. & Crick, F. H. C. Molecular structure of nucleic acids: a structure for deoxyribose nucleic acid. *Nature* **171**, 737–738 (1953).
 - [2] Prelog, V. Chirality in chemistry. *Science* **193**, 17–24 (1976).
 - [3] Nugent, W. A., RajanBabu, T. V. & Burk, M. J. Beyond nature’s chiral pool: Enantioselective catalysis in industry. *Science* **259**, 479–483 (1993).
 - [4] Lee, T. D. & Yang, C. N. Question of parity conservation in weak interactions. *Phys. Rev.* **104**, 254–258 (1956).
 - [5] Wu, C. S., Ambler, E., Hayward, R. W., Hoppes, D. D. & Hudson, R. P. Experimental test of parity conservation in beta decay. *Phys. Rev.* **105**, 1413–1415 (1957).
 - [6] Rikken, G. L. J. A. & Raupach, E. Enantioselective magnetochiral photochemistry. *Nature* **405**, 932–935 (2000).
 - [7] Pendry, J. B. A chiral route to negative refraction. *Science* **306**, 1353–1355 (2004).
 - [8] Tang, Y. & Cohen, A. E. Optical chirality and its interaction with matter. *Phys. Rev. Lett.* **104**, 163901 (2010).
 - [9] Muhlbauer, S. et al. Skyrmion lattice in a chiral magnet. *Science*, **323**, 915–919 (2009).
 - [10] Yu, X.-Z. et al. Real-space observation of a two-dimensional skyrmion crystal. *Nature* **465**, 901–904 (2010).
 - [11] Rikken, G. L. J. A., Fölling, J. & Wyder, P. Electrical magnetochiral anisotropy. *Phys. Rev. Lett.*

- 87**, 236602 (2001).
- [12] Nakatsuji, S., Kiyohara, N. & Higo, T. Large anomalous Hall effect in a non-collinear antiferromagnet at room temperature. *Nature* **527**, 212–215 (2015).
- [13] Chang, G. et al. Topological quantum properties of chiral crystals. *Nat. Mater.* **17**, 978–985 (2018).
- [14] Gooth, J. et al. Axionic charge-density wave in the Weyl semimetal $(\text{TaSe}_4)_2\text{I}$. *Nature* **575**, 315–319 (2019).
- [15] Szasz, A., Motruk, J., Zaletel, M. P. & Moore, J. E. Chiral spin liquid phase of the triangular lattice Hubbard model: a density matrix renormalization group study. *Phys. Rev. X* **10**, 021042 (2020).
- [16] Liu, Y., Xiao, J., Koo, J. & Yan, B. Chirality-driven topological electronic structure of DNA-like materials. *Nat. Mater.* **20**, 638–644 (2021).
- [17] Hasan, M. Z. et al. Weyl, Dirac and high-fold chiral fermions in topological quantum matter. *Nat. Rev. Mater.* **6**, 784–803 (2021).
- [18] Yang, S.-H., Naaman, R., Paltiel, Y. & Parkin, S. S. Chiral spintronics. *Nat. Rev. Phys.* **3**, 328–343 (2021).
- [19] Wang, X., Yi, C. & Felser, C. Chiral quantum materials: when chemistry meets physics. *Adv. Mater.* **36**, 2308746 (2023).
- [20] Li, J. et al. Signatures of polarized chiral spin disproportionation in rare earth nickelates. *Nat. Commun.* **15**, 7427 (2024).
- [21] Guo, C. et al. Distinct switching of chiral transport in the kagome metals KV_3Sb_5 and CsV_3Sb_5 . *Nat. Commun.* **9**, 20 (2024).
- [22] Ishioka, J. et al. Chiral charge-density waves. *Phys. Rev. Lett.* **105**, 176401 (2010).
- [23] van Wezel, J. Chirality and orbital order in charge density waves. *Europhys. Lett.* **96**, 67011 (2011).
- [24] Vaskivskiy, I. et al. Fast electronic resistance switching involving hidden charge density wave states. *Nat. Commun.* **7**, 11442 (2016).
- [25] Zong, A. et al. Ultrafast manipulation of mirror domain walls in a charge density wave. *Sci. Adv.* **4**, eaau5501 (2018).
- [26] Xu, S.-Y. et al. Spontaneous gyrotropic electronic order in a transition-metal dichalcogenide. *Nature* **578**, 545–549 (2020).
- [27] Yang, H. F. et al. Visualization of chiral electronic structure and anomalous optical response in a material with chiral charge density waves. *Phys. Rev. Lett.* **129**, 156401 (2022).
- [28] Liu, G. et al. Electrical switching of ferro-rotational order in nanometre-thick 1T-TaS₂ crystals.

- Nat. Nanotechnol.* **18**, 854–860 (2023).
- [29] Zhao, Y. et al. Spectroscopic visualization and phase manipulation of chiral charge density waves in 1T-TaS₂. *Nat. Commun.* **14**, 2223 (2023).
- [30] Jiang, Y.-X. et al. Unconventional chiral charge order in kagome superconductor KV₃Sb₅. *Nat. Mater.* **20**, 1353–1357 (2021).
- [31] Wang, Z. et al. Electronic nature of chiral charge order in the kagome superconductor CsV₃Sb₅. *Phys. Rev. B* **104**, 075148 (2021).
- [32] Guo, C. et al. Switchable chiral transport in charge-ordered kagome metal CsV₃Sb₅. *Nature* **611**, 461–466 (2022).
- [33] Yang, S.-Y. et al. Giant, unconventional anomalous Hall effect in the metallic frustrated magnet candidate, KV₃Sb₅. *Sci. Adv.* **6**, eabb6003 (2020).
- [34] Grüner, G. The dynamics of charge-density waves. *Rev. Mod. Phys.* **60**, 1129 (1988).
- [35] Tan, H., Liu, Y., Wang, Z. & Yan, B. Charge density waves and electronic properties of superconducting kagome metals. *Phys. Rev. Lett.* **127**, 046401 (2021).
- [36] Subedi, A. Hexagonal-to-base-centered-orthorhombic 4Q charge density wave order in kagome metals KV₃Sb₅, RbV₃Sb₅, and CsV₃Sb₅. *Phys. Rev. Mater.* **6**, 015001 (2022).
- [37] Subedi, A. Trigonal-to-monoclinic structural transition in TiSe₂ due to a combined condensation of $q=(1/2, 0, 0)$ and $(1/2, 0, 1/2)$ phonon instabilities. *Phys. Rev. Mater.* **6**, 014602 (2022).
- [38] Li, H. et al. Observation of unconventional charge density wave without acoustic phonon anomaly in kagome superconductors AV₃Sb₅ (A= Rb, Cs). *Phys. Rev. X* **11**, 031050 (2021).
- [39] Ortiz, B. R. et al. Fermi surface mapping and the nature of charge-density-wave order in the kagome superconductor CsV₃Sb₅. *Phys. Rev. X* **11**, 041030 (2021).
- [40] Xiao, Q. et al. Coexistence of multiple stacking charge density waves in kagome superconductor CsV₃Sb₅. *Phys. Rev. Res.* **5**, L012032 (2023).
- [41] Li, H. et al. Rotation symmetry breaking in the normal state of a kagome superconductor KV₃Sb₅. *Nat. Phys.* **18**, 265–270 (2022).
- [42] Zhao, H. et al. Cascade of correlated electron states in the kagome superconductor CsV₃Sb₅. *Nature* **599**, 216–221 (2021).
- [43] Xiang, Y. et al. Twofold symmetry of c-axis resistivity in topological kagome superconductor CsV₃Sb₅ with in-plane rotating magnetic field. *Nat. Commun.* **12**, 6727 (2021).
- [44] Jiang, K. et al. Kagome superconductors AV₃Sb₅ (A= K, Rb, Cs). *Natl. Sci. Rev.* **10**, nwac199 (2023).
- [45] Song, X. et al. Atomic-scale visualization of chiral charge density wave superlattices and their reversible switching. *Nat. Commun.* **13**, 1843 (2022).

- [46] Togo, A. & Tanaka, I. First principles phonon calculations in materials science. *Scr. Mater.* **108**, 1–5 (2015).
- [47] Ortiz, B. R. *et al.* New kagome prototype materials: discovery of KV_3Sb_5 , RbV_3Sb_5 , and CsV_3Sb_5 . *Phys. Rev. Mater.* **3**, 094407 (2019).

Acknowledgments

Work at Nanyang Technological University was supported by the National Research Foundation, Singapore, under its Fellowship Award (NRF-NRFF13-2021-0010), the Agency for Science, Technology and Research (A*STAR) under its Manufacturing, Trade and Connectivity (MTC) Individual Research Grant (IRG) (Grant No.: M23M6c0100), the Singapore Ministry of Education (MOE) Academic Research Fund Tier 3 grant (MOE-MOET32023-0003), Singapore Ministry of Education (MOE) AcRF Tier 2 grant (MOE-T2EP50222-0014) and the Nanyang Assistant Professorship grant (NTU-SUG). The computational work for this article was partially performed on resources of the National Supercomputing Centre, Singapore (<https://www.nscg.sg>). The work at Northeastern University was supported by the National Science Foundation through NSF-ExpandQISE award #2329067 and benefited from the resources of Northeastern University's Advanced Scientific Computation Center, the Discovery Cluster, and the Massachusetts Technology Collaborative. M.Z.H. group acknowledges primary support from the US Department of Energy (DOE), Office of Science, National Quantum Information Science Research Centers, Quantum Science Center (at ORNL) and Princeton University; STM Instrumentation support from the Gordon and Betty Moore Foundation (GBMF9461) and the theory work; and support from the US DOE under the Basic Energy Sciences programme (grant number DOE/BES DE-FG-02-05ER46200) for the theory and sample characterization work including ARPES. C.-L. Zhang was supported by the National Key R&D Program of China (Grant No. 2023YFA1407400) and a start-up grant from the Institute of Physics, Chinese Academy of Sciences. Q.M. and S.-Y.X. acknowledge support from the Center for the Advancement of Topological Semimetals, an Energy Frontier Research Center funded by the US Department of Energy Office of Science, through the Ames Laboratory under contract DE-AC02-07CH11358.

Competing interests The authors declare no competing interests.

FIGURES

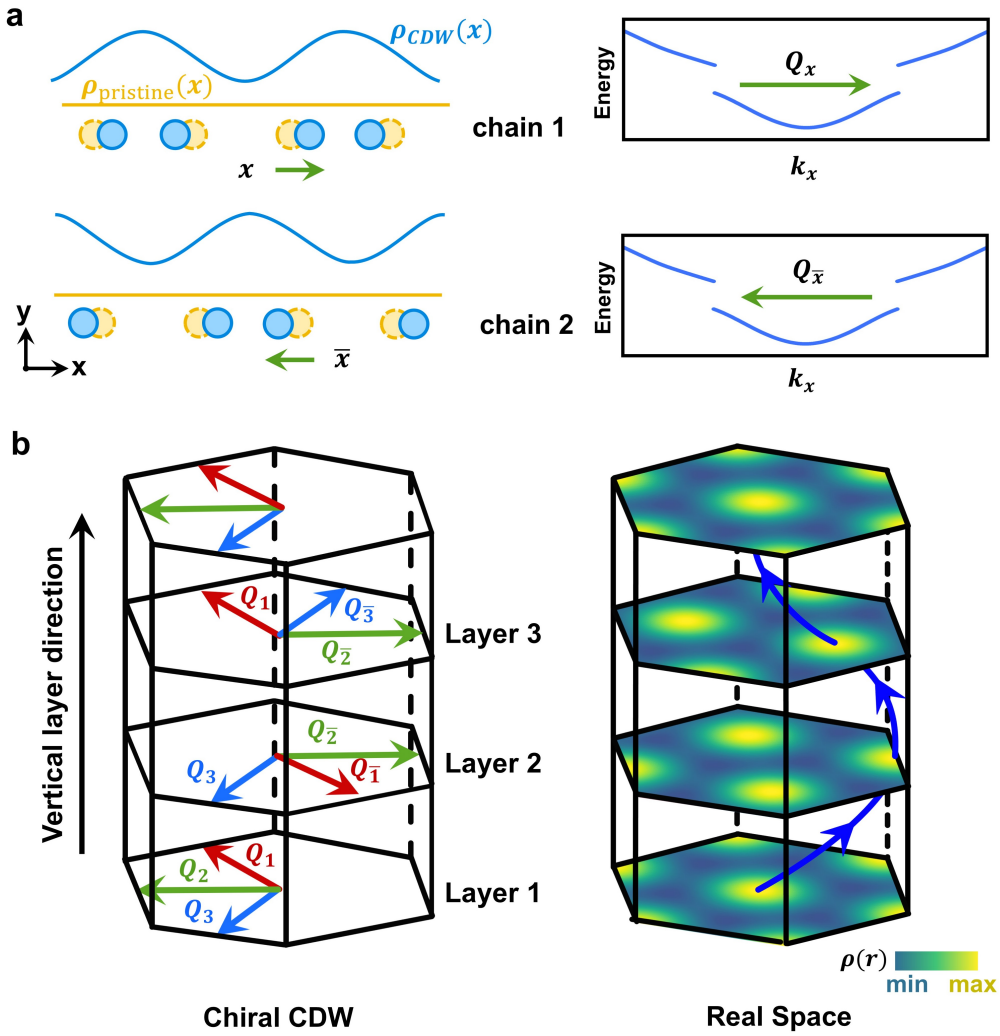


FIG. 1. **Mechanism for inducing structural chirality via CDW.** **a**, Schematic of a quasi-1D structural transition induced by CDW. The orange and blue circles correspond to atomic positions in the original cell and CDW cell, respectively. Q_x and $Q_{\bar{x}}$ denotes Q-vectors with opposite phases, indicating opposite atomic displacement of CDW in real space. **b**, Left: Visualization of spiral Q-vectors with phase differences across layers. Right: Illustration of the charge distribution associated with the spiral Q-vectors shown on the left.

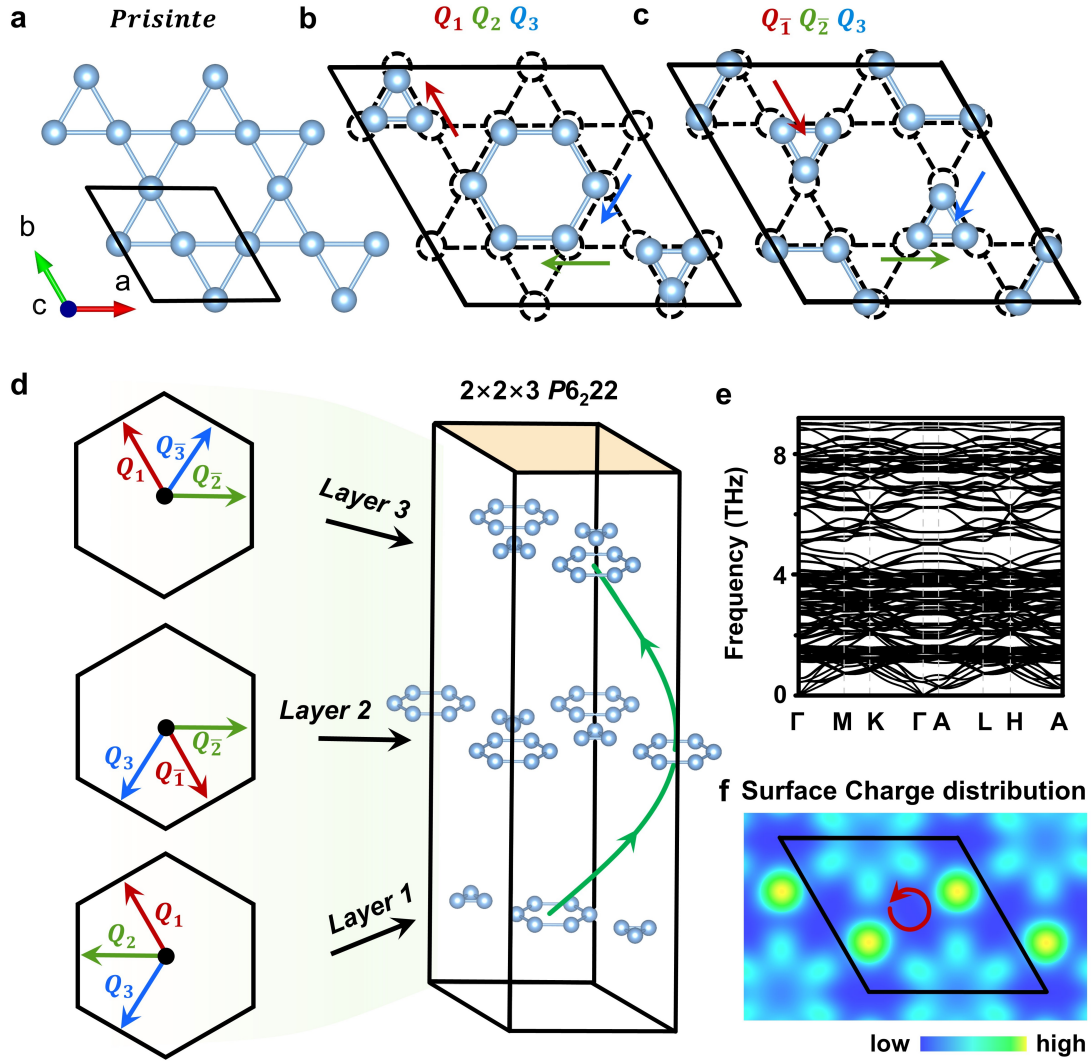


FIG. 2. Prediction of structural chirality in the CDW phase of AV_3Sb_5 ($A = K, Rb,$ and Cs). **a**, A $2 \times 2 \times 1$ supercell of the pristine phase, with the primitive cell outlined by the black solid line. **b-c**, Inverse star of David patterns resulting from $Q_1 Q_2 Q_3$ and $Q_{\bar{1}} Q_2 Q_3$, respectively. The black dashed lines represent the ideal kagome lattice. Schematic atomic displacements induced by $Q_1/Q_{\bar{1}}$, $Q_2/Q_{\bar{2}}$, and $Q_3/Q_{\bar{3}}$ are denoted by red, blue, and green arrows, respectively. **d**, Illustration of how to generate chiral CDW structure. The incorporation of pattern $Q_1 Q_2 Q_3$, $Q_{\bar{1}} Q_2 Q_3$ and $Q_1 Q_2 Q_{\bar{3}}$ forms a chiral $2 \times 2 \times 3$ CDW with the space group of $P6_222$. The green curve shows the helical arrangement for the centre of ISD patterns from the bottom to the top. **e**, Phonon spectrum of $2 \times 2 \times 3$ chiral CDW. **f**, Simulated surface charge distribution on the Sb surface, highlighted as the light orange region in (d).

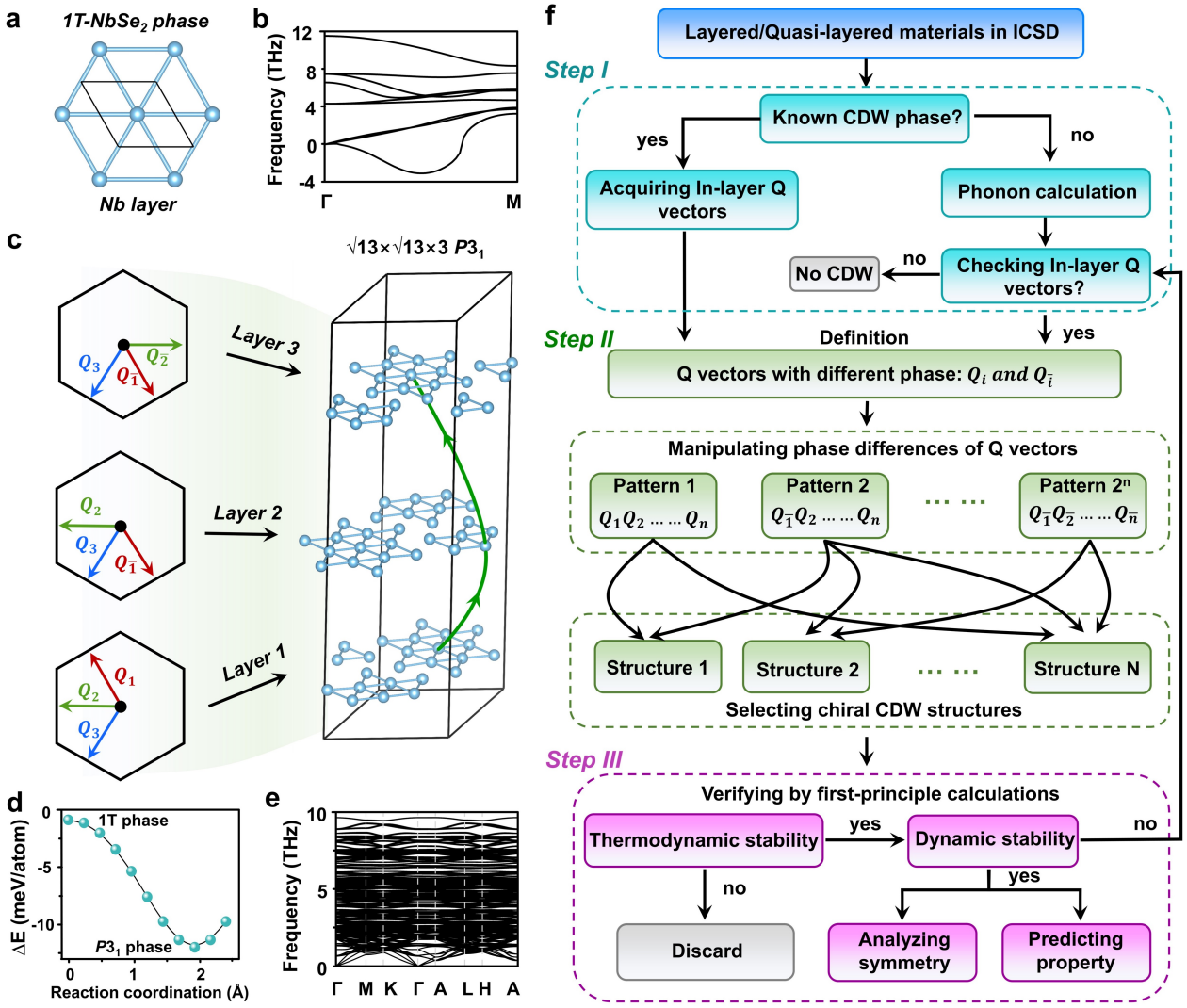


FIG. 3. **Framework for predicting Chiral CDW via DFT.** **a**, Nb layer in the pristine phase of 1T-NbSe₂. **b**, Phonon spectrum of 1T-NbSe₂ pristine phase. **c**, Illustration of generating a chiral CDW structure: combining $Q_1 Q_2 Q_3$, $Q_{\bar{1}} Q_2 Q_3$ and $Q_{\bar{1}} Q_{\bar{2}} Q_3$ forms a chiral $\sqrt{13} \times \sqrt{13} \times 3$ CDW with the space group of $P3_1$. The green curve shows the helical arrangement for the centre of SoD patterns from the bottom to the top. **d**, Reaction path between between the pristine phase and the chiral CDW phase, where the lower energy indicates the thermodynamic stability of the chiral CDW phase. **e**, Phonon spectrum of chiral $\sqrt{13} \times \sqrt{13} \times 3$ CDW phase, with no negative frequencies indicating dynamic stability. **f**, General framework for predicting chiral CDW phases of layered/quasi-layered materials in ICSD database.

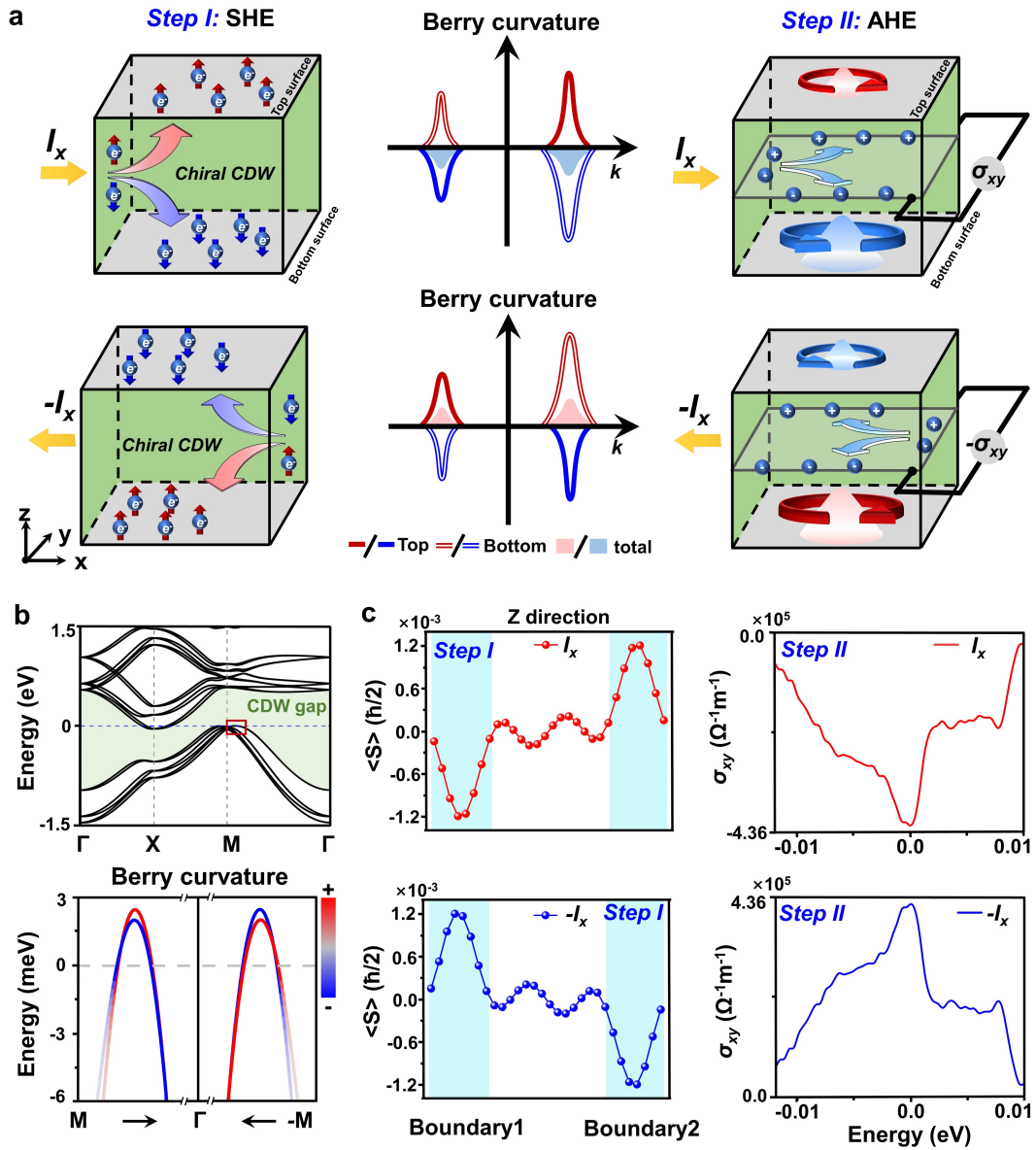


FIG. 4. **Theoretical prediction of spin-anomalous dual-Hall effect in chiral CDWs.** **a**, Schematic illustration of the correlation-driven spin-anomalous dual-Hall effect in nonmagnetic chiral CDW materials. Step I represents the spin Hall effect (SHE) generated by current injection along the x -direction in the chiral CDW system. The middle panel shows the Berry curvature distributions on the top and bottom surfaces, induced by spin accumulation and the chiral CDW, which break P , T , and PT symmetries. The imbalance distribution of Berry curvature on the top and bottom surface induces the AHE, as shown in Step II. The top and bottom panels illustrate two scenarios of the dual-Hall effect with opposite current directions. **b**, Band structure of tight-band models in $2 \times 2 \times 3$ supercell with chiral CDW. The lower panel shows the Berry curvature distribution along the M - Γ and Γ - $(-M)$ paths, with red and blue markers indicating opposite signs of Berry curvature. **c**, Left panel: Simulated spin accumulation of each layer along the z -direction with I_x and $-I_x$ current injections. The cyan regions indicate the slab boundary layers. Right panel: Anomalous Hall conductivity σ_{xy} for I_x and $-I_x$ current injections.

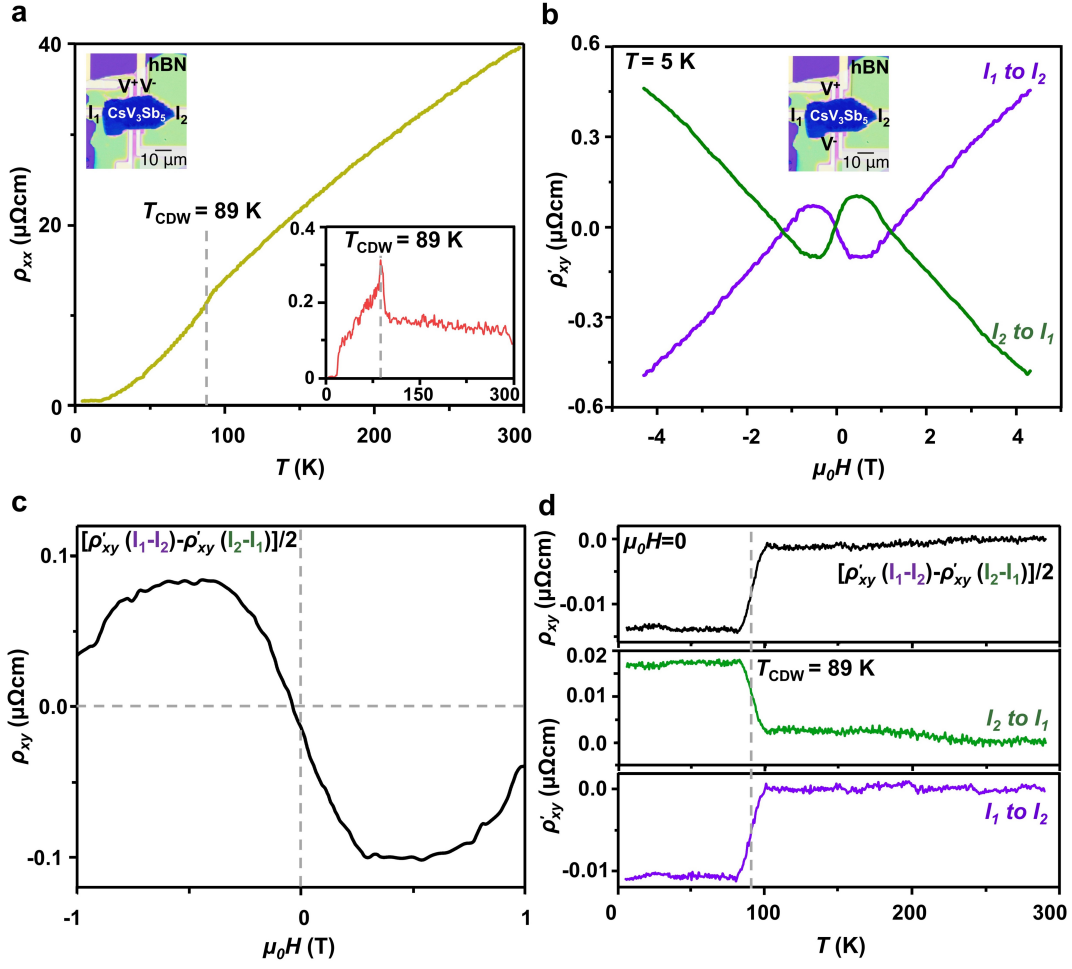


FIG. 5. **Experimental observation of a zero-field non-zero Hall effect attributable to chiral CDW.** **a**, Four-probe longitudinal resistivity (ρ_{xx}) of a mechanically exfoliated ~ 90 nm thick CsV₃Sb₅ crystal as a function of the temperature (T), showing a CDW transition near $T=T_{CDW} \simeq 89$ K. The top inset shows an optical image of the device, with a CsV₃Sb₅ flake encapsulated in a hexagonal boron nitride (h-BN) layer, highlighting the current (I_1 and I_2) and voltage (V^+ and V^-) leads. The bottom inset depicts the derivative of the ρ_{xx} as a function of T . Here the CDW transition manifests as a sharp peak in $(d\rho_{xx})/dT$ (T). **b**, Raw transverse resistivity (ρ'_{xy}) data measured using the Hall configuration (shown in the inset) at $T \simeq 5$ K. The data is presented as a function of the magnetic field ($\mu_0 H$). The color-coded curves represent this raw, unsymmetrized ρ'_{xy} ($\mu_0 H$) for two opposite current flow directions, from I_1 and I_2 and I_2 to I_1 leads. Inset shows the contact configuration on the device for measuring ρ_{xy} . **c**, Hall resistivity (ρ_{xy}) as a function of $\mu_0 H$ obtained via subtracting ρ'_{xy} ($\mu_0 H$) values for opposite current directions and dividing the result by two. ρ_{xy} is clearly non-zero at $\mu_0 H = 0$. **d**, Temperature dependence of ρ'_{xy} for both current directions, and ρ_{xy} (calculated similarly to panel c). All three traces show pronounced transitions around T_{CDW} . ρ'_{xy} and ρ_{xy} are all close to zero prior to the CDW transition as one might expect. Strikingly, below T_{CDW} , a finite, non-zero Hall resistivity is seen at zero field.